


Ultrabroadband Acoustic Ventilation Barriers via Hybrid-Functional Metasurfaces

Ruizhi Dong,^{1,‡} Dongxing Mao,^{1,‡} Xu Wang,^{1,2,*} and Yong Li^{1,2,†}

¹*Institute of Acoustics, School of Physics Science and Engineering, Tongji University, 200092 Shanghai, China*

²*College of Architecture and Urban Planning, Tongji University, 200092 Shanghai, China*

 (Received 25 October 2020; revised 29 December 2020; accepted 2 February 2021; published 18 February 2021)

Ventilation barriers allowing simultaneous sound blocking and free airflow passage are a great challenge but are necessary for particular scenarios calling for soundproofing ventilation. Previous studies using local resonance or Fano-like interference consider a narrow working range around the resonant or destructive-interference frequency. Efforts made with regard to broadband designs show a limited bandwidth typically smaller than half an octave. Here we conceptually propose an ultrabroadband ventilation barrier via hybridization of dissipation and interference. Confirmed by experiments, our hybrid-functional metasurface, empowered by its synergistic effect, significantly expands the range of the operating frequencies, enabling an effective blocking of more than 90% of incident energy in the range from 650 to 2000 Hz, while its structural thickness is only 53 mm (approximately $\lambda/10$). Our design showcases the great flexibility of customizing the broadband and is capable of tackling sound coming from various directions, which has potential in air-permeable yet soundproofing applications.

DOI: [10.1103/PhysRevApplied.15.024044](https://doi.org/10.1103/PhysRevApplied.15.024044)

I. INTRODUCTION

In acoustic engineering, there remains a significant challenge for simultaneous soundproofing and free flow passage. For example, from the perspective of green buildings, it is encouraged to open windows for natural ventilation. However, the inevitably accompanying “invasive” noise is usually annoying. Acoustic barriers such as closed windows impede airflow, while conventional ventilation barriers with winding airflow paths with absorptive linings bring about a large pressure drop and hence cannot maintain a free flow of air [1–3]. Acoustic metasurfaces, as a research area that has attracted increasing attention, have showcased their unparalleled capabilities in tailoring the wave-matter interaction and created unprecedented opportunities in sound-field manipulation at the deep-subwavelength level, exemplified by subwavelength focusing or imaging [4,5], one-way sound transportation [6,7], anomalous refraction and reflection [8–19], and compact absorbers [20–24]. In light of its exceptional success, an acoustic metasurface offers an efficient means to design air-permeable barriers, spawning hollow-carved-board designs consisting of periodically arranged hollow units to ensure sufficient air circulation. By leveraging local resonances [25–30] (Helmholtz resonators,

membranes, quarter-wavelength tubes, etc.) or Fano-like interferences [31–33], they break the limitations of regulating large-scale waves at subwavelength scales and enable sound impedance in such an unprecedented open way. Despite this, the underlying working mechanism implies that they serve narrow working-frequency ranges around the resonant or destructive-interference frequencies. Initial efforts to broaden the working frequency range showed either a limited bandwidth [29] or a largely degraded airflow passage [34]. It was shown recently that by coupling multiple lossy resonators, a ventilation barrier can achieve broadband absorption at low frequencies [35,36]. Besides, a barrier made from hollow helical units offers consistent quasi-Fano-like interference and hence a broadband insulation in the mid-high frequency range [37]. Although these designs [35,37] show remarkable progress in dealing with the broadband issue, the bandwidths are still limited, and are usually smaller than half an octave if evaluated by the measure of blocking more than 90% of incident energy [30].

Considering that noise usually covers a wide spectrum, designing an ultrabroadband ventilation barrier is still being pursued. Here, by harnessing the hybridization of dissipation and interference, we conceptually propose and experimentally demonstrate a ventilation barrier capable of exceptionally broadband sound blocking. The designed metaunit is a hollowed-out cylinder, akin to the profile in our previous work [37], with almost the same outer and inner diameters as well as total thickness. However, in

*xuwang@tongji.edu.cn

†yongli@tongji.edu.cn

‡These authors contributed equally to this work.

contrast to the design in Ref. [37], which relies entirely on interference, here dissipation is induced by coupled lossy chambers, which effectively lowers the operating range. Together with other coupled reactance chambers, a hybrid-functional open metasurface is achieved in this work. Empowered by the synergistic effect, the scope of its working frequencies is significantly expanded. Such a barrier effectively blocks more than 90% of incident sound energy in the range from 628 to 1400 Hz coming from various directions, while the structural thickness is only 53 mm (approximately $\lambda/10$). By adding circumferential partitions to the metaunit, we further achieve an expanded bandwidth (90% sound-energy insulation in the range from 650 to 2000 Hz). Our design suggests an efficient approach toward noise-control engineering in flowing-fluid-filled situations.

II. RESULTS AND DISCUSSION

A. The ventilation barrier for broadband sound blocking

Figure 1(a) shows a conceptual view of the designed ventilation barrier, of which the building block is a hollowed-out cylinder with eight stacked functional layers, as schematically illustrated in Fig. 1(b). For clarity, the first layer is detached to show the details of its inner structure. Each layer is split into two resonant chambers, with the same opening areas but different chamber lengths, which are separated by a deflected blade. To leverage the coherent coupling for the broadband issue [24], the openings of

the resonant chambers are adjacent to each other (opening area of the resonant chambers S_n). The geometries of the eight layers are the same, except that the deflected angles are gradually shifted (angle of the first-layer partition ψ , angle shift from layer to layer θ), resulting in the whole structure being composed of 16 elaborately detuned resonant chambers. As shown in the following, these resonant chambers are conceived explicitly so that each makes its own contribution (highly efficient dissipation or interference), and they collectively provide a remarkable sound blocking over a wide frequency range, while the whole structure features a subwavelength thickness. The detailed geometry of the design metaunit is illustrated in Fig. 1(b), involving outer diameter D , inner diameter d , and thickness of the unit chamber h . The thickness of the inner and outer cylindrical shells, the top and bottom plates, and the partition blades is b . The overall thickness of the metaunit is H ($H = 8h + 9b$).

B. The effective model of the ventilation barrier

The acoustic performance of the proposed metaunit can be characterized by its transfer matrix \mathbf{T}_0 , which relates the state vectors of the sound fields at the input and output parts across the metaunit, as $\{p, v\}_{\text{in}}^T = \mathbf{T}_0 \{p, v\}_{\text{out}}^T$. The overall performance of the metaunit is attributed to both the cross-section changes at the input and output interfaces and the 16 side-branched resonant chambers. Moreover, although the resonant chambers are stacked layer by layer [the center height of the resonant chamber n_{\pm} shown in Fig. 1(b) can be written as $z_n = (9 - n)b +$

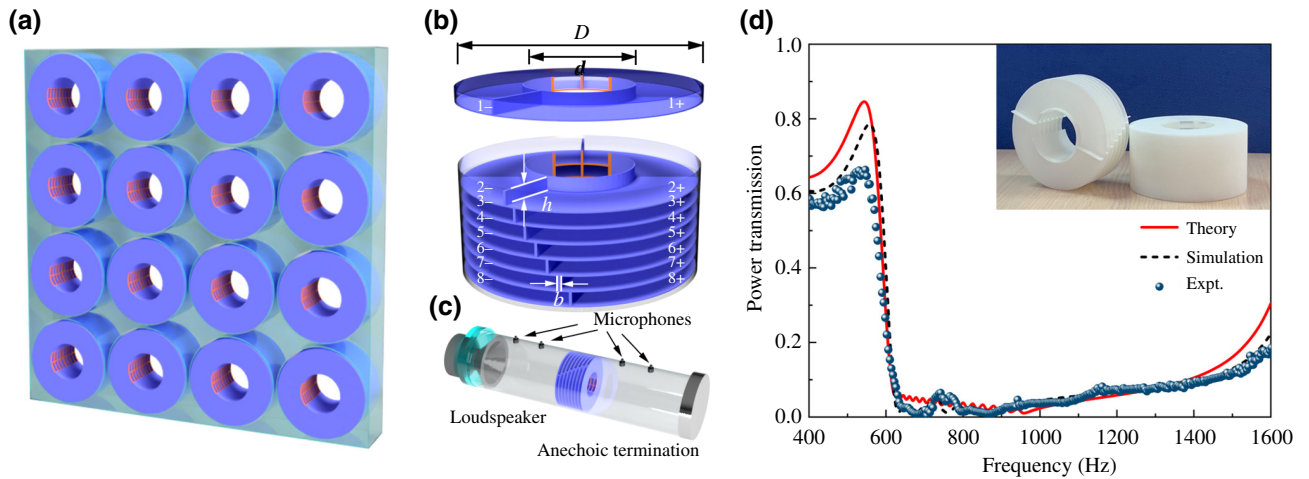


FIG. 1. (a) Conceptual view of the broadband ventilation barrier consisting of periodically arranged metaunits. (b) The designed metaunit is composed of eight layers. Each layer is split into two resonant chambers by a deflected blade (the first layer is removed to show the inner details). Here the cylindrical metaunit is designed as prescribed by the standard impedance tube for experiments. With the presented design strategy being followed, it can be straightforwardly reshaped as a cube and then periodically arranged to form a barrier. (c) Experimental setup, where the specimen is clamped in the impedance tube. (d) Theoretical (red line), simulated (black dashed line), and measured (blue dots) acoustic power transmission of the designed metaunit with $D = 100$ mm, $d = 44$ mm, $h = 5.5$ mm, $b = 1$ mm, $H = 53$ mm, $\psi = 142.5^\circ$, $\theta = 5^\circ$, and $S_n = 63.4$ mm². The inset shows an enlarged view of a three-dimensionally-printed specimen of the designed metaunit (right) and its inner structure (left).

$(8.5 - n)h$, $n = 1, 2, \dots, 8$], owing to the subwavelength nature of the metaunit (so the separation of these chambers is on a deep-subwavelength scale), one can further assume that all these resonant chambers share the same location at the half-height of the metaunit (i.e., $z_n = H/2$, $n = 1, 2, \dots, 8$). Therefore, the transfer matrix \mathbf{T}_0 can be written as $\mathbf{T}_0 = \mathbf{T}_f \mathbf{T}_a \mathbf{T}_r$. Hypothetically, this is equivalent to a rigid-walled shrunken-cross-section tube (height H), with all these resonant chambers now mounted around its bisecting plane. Here the matrix \mathbf{T}_f (\mathbf{T}_r) describes the contribution of cross-section mutation of the first (last) half the changeable-cross-section tube, which is given by

$$\mathbf{T}_f (\mathbf{T}_r) = \begin{pmatrix} \cos k_0 L_c & j \sin k_0 L_c / \phi_0 \\ j \phi_0 \sin k_0 L_c & \cos k_0 L_c \end{pmatrix}, \quad (1)$$

where k_0 is the wave number of acoustic waves in air, ϕ_0 denotes the ratio of the open area in the metaunit ($\phi_0 = d^2/D^2$), and $L_c = 0.5H + \Delta H$ is the effective length of the first or latter half the changeable-cross-section tube taking into account the end correction ΔH . Here the end correction can be set as $\Delta H = 0.425d(1 - 1.25\sqrt{\phi_0})$ by considering the radiation impedance due to the change in cross section in the process of sound propagation [22]. The matrix \mathbf{T}_a represents the contribution from the ensemble of the 16 resonant chambers. Such an aggregate supports a strong coherent coupling effect, so it can be treated as an overall coupled system whose acoustic impedance can be calculated as follows. First, one can define the acoustic impedance of each individual resonant chamber with reference to the overall coupled system by replacing all other resonant chambers with hard walls. In this way, the acoustic impedance of the resonant chamber n_{\pm} with reference to the overall coupled system can be expressed as $Z_{n_{\pm}} = -j \rho_c c_c \cot k_c L_{n_{\pm}} / \xi \rho c$ [24], where k_c , ρ_c , and c_c are the wave number, air density, and sound speed in the resonant chambers, respectively. Because of the intrinsic loss induced by viscous and thermal boundary layers in these narrow chambers, these parameters (k_c , ρ_c , c_c) are now complex. L_{n_+} and L_{n_-} are the effective lengths of the resonant chambers n_+ and n_- , and ξ is the ratio of the cross-section area of the resonant chamber to its opening area. Then we can obtain the overall acoustic impedance of these 16 resonant chambers as

$$Z_a = \left[\sum \frac{h}{2H} \left(\frac{1}{Z_{n_+}} + \frac{1}{Z_{n_-}} \right) \right]^{-1} \quad (n = 1, 2, \dots, 8). \quad (2)$$

Equation (2) gives the impedance of the 16 coherently coupled resonant chambers. By further considering the cross-section area of the changeable-cross-section tube S and the total opening area of all resonant chambers S_a ($S_a = 16S_n$), we can express \mathbf{T}_a as

$$\mathbf{T}_a = \begin{pmatrix} 1 & 0 \\ S_a/SZ_a & 1 \end{pmatrix}. \quad (3)$$

On the basis of Eqs. (1) and (3), the transfer matrix \mathbf{T}_0 for the designed metaunit is finally derived. Then the power transmission τ of the metaunit can be straightforwardly predicted by the formula

$$\tau = (2/|t_{11} + t_{12} + t_{21} + t_{22}|)^2, \quad (4)$$

where t_{ij} ($i, j = 1, 2$) represents the elements of the matrix \mathbf{T}_0 .

C. Numerical simulations and experimental demonstration of the ventilation barrier

The designed metaunit is numerically simulated by our using the pressure acoustic module of COMSOL Multiphysics, in which a frequency-domain study is performed to calculate the sound transmission through the metaunit. To estimate its low-frequency behavior under plane-wave incidence, the designed metaunit is placed in a cylindrical waveguide, and both the waveguide wall and the metaunits are considered acoustically rigid. Both ends of the waveguide are set as plane-wave radiation boundaries, while the incident wave is excited at only one side. To take the losses arising from the viscous and thermal dissipation into consideration, the narrow-region acoustics model is used in these resonant chambers.

The experiment is performed to verify the designed metaunit. The transfer-matrix method is adopted to measure the power transmission of the metaunit by use of a Sinus type-1401 impedance tube, where the sample is fixed firmly with clamps in the impedance tube. The experimental setup, which is consistent with that adopted in numerical modeling, is schematically illustrated in Fig. 1(c). The sample of the metaunit made of photosensitive resin via three-dimensional (3D) printing is shown in the inset in Fig. 1(d).

Figure 1(d) shows the power transmission of the metaunit. The theoretical prediction shows excellent agreement with numerical and experimental results, demonstrating the effectiveness of our design. Such a ventilation barrier blocks more than 90% of incident sound energy, that is, 10 dB in transmission loss (transmission loss $T_L = -10 \log \tau$), in the range from 628 to 1400 Hz (experimental data). Note that the designed metaunit has a profile very similar to the design in previous work [37]. Both are hollowed-out-cylinder designs with almost the same outer and inner diameters as well as total thickness. However, the capability of the current design (metaunit $T_L > 10$ dB in the range from 628 to 1400 Hz) is substantially superior to that of its counterpart ($T_L > 10$ dB in the range of approximately 900 to 1400 Hz). More specifically, harnessing the power of dissipation in combination with interference remarkably lowers the onset frequency in the current design.

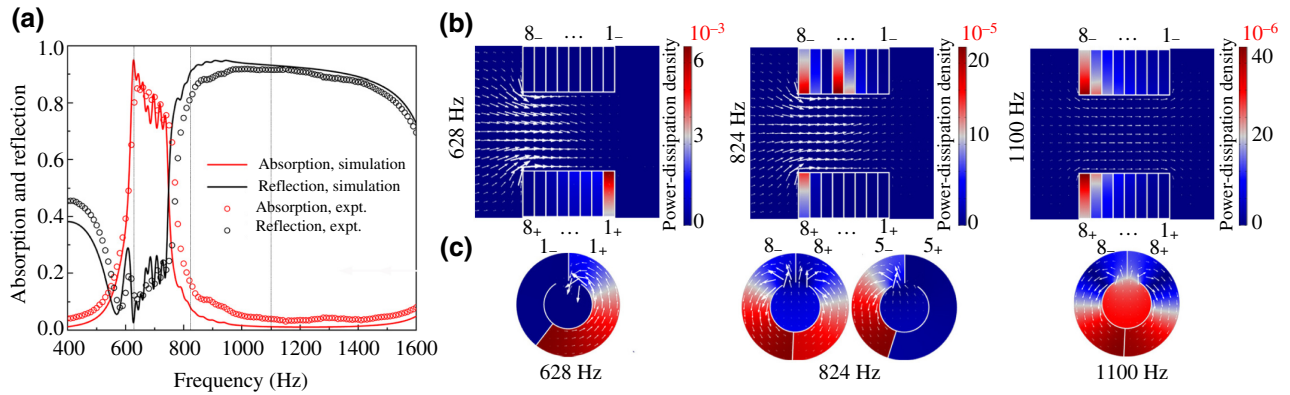


FIG. 2. (a) Numerically calculated absorption (red line) and reflection (black line) and measured absorption (red circle) and reflection (black circle) of the metaunit. The dashed gray lines refer to three representative frequencies, where the performance of the metaunit is dominated by absorption (628 Hz), absorption and interference (824 Hz), and interference (1100 Hz). (b) Axial-plane view of the simulated sound-field distributions at the three marked frequencies. The colors illustrate the power-dissipation density, and the arrows represent the energy-flow distribution. (c) Radial-plane view of the specific layers where the “active” resonators are located. The color illustrates the acoustic pressure distributions, and the arrows represent the local-velocity streamlines.

D. The working mechanism of the ventilation barrier

The capability of the designed metaunit for broadband sound blocking has been demonstrated. To further explore the underlying working mechanism, the absorption and reflection of the metaunit are numerically calculated and experimentally measured, as shown by Fig. 2(a). This reveals that such a wide working range is achieved via the synergy of absorption and reflection (i.e., a hybridized effect of dissipation and interference). Here we consider three representative frequency points (628, 824, and 1100 Hz), at which the performance of the metaunit is dominated by absorption, absorption-reflection coaction, and reflection, respectively. Figure 2(b) shows the numerical results for the sound field in the axial-plane view of the metaunit at these representative frequencies, where the color maps illustrate the power-dissipation density. The red color highlights those “active” chambers (i.e. the chambers under strong resonance) at these frequencies. Note that the maximum value of the color bar clarifies the underlying working mechanism. At 628 Hz, the active unit (chamber 1_+) provides the highest dissipation density (approximately 10^{-3}), indicating a strong energy dissipation and a prominent absorption effect (the first inset). At 824 Hz, the active units (chambers 8_+ and 8_-) show a much lower dissipation density (approximately 10^{-5}), so the metaunit works by the coaction of absorption and reflection [the second inset in Fig. 2(b)]. At 1100 Hz, the dissipation density of the active units (approximately 10^{-6}) is 3 orders of magnitude lower than that at 628 Hz, implying that these active units support little sound absorption but strong reflection (the third inset). The white arrows in Fig. 2(b) represent the sound intensity, showing the energy-flow distribution when sound is passing through the metaunit (from left

to right). At 628 Hz, the obvious arrows at the input of the metaunit gradually decay and finally disappear at the output, showing a strong energy dissipation through the metaunit. However, at 1100 Hz, the diminished arrows at the input stem from the cancellation of quasiequal strength of incident and reflected flux traveling in opposite directions. This is clear evidence that now the metaunit behaves as a strong reflector, while the contribution to absorption is negligible. When the metaunit provides a hybridized function (824 Hz), the distribution of sound intensity presents a pattern in between the former two extremes, as illustrated by the second inset in Fig. 2(b). Even more notably, in these three cases, the arrows diminished at the output demonstrate the consistently strong sound blocking at these frequencies.

Figure 2(c) shows a cross-section view of the sound field in the layers where the actively working chambers are located. Note that now the color maps and the arrows illustrate the sound pressure and local-particle-velocity distribution, respectively. Compared with the inactive chambers (e.g., chamber 1_- at 824 Hz), the obvious arrows in the active chambers witness a massive energy exchange occurs between the chamber and outer space, and the sound-pressure distribution demonstrates energy accumulation at the chamber terminals, both proving a state of resonance.

In essence, there are two factors determining the open metaunit composed of detuned chambers blocking the acoustic wave. One is whether the incident wave can be induced in the chambers adequately, and the other is whether it can be sufficiently dissipated in the chambers. When a chamber is in the resonant state (so that the incident sound wave interacts strongly with the chamber) and has an adequate dissipation rate, the chamber shows remarkable absorption capacity, seen as a state of

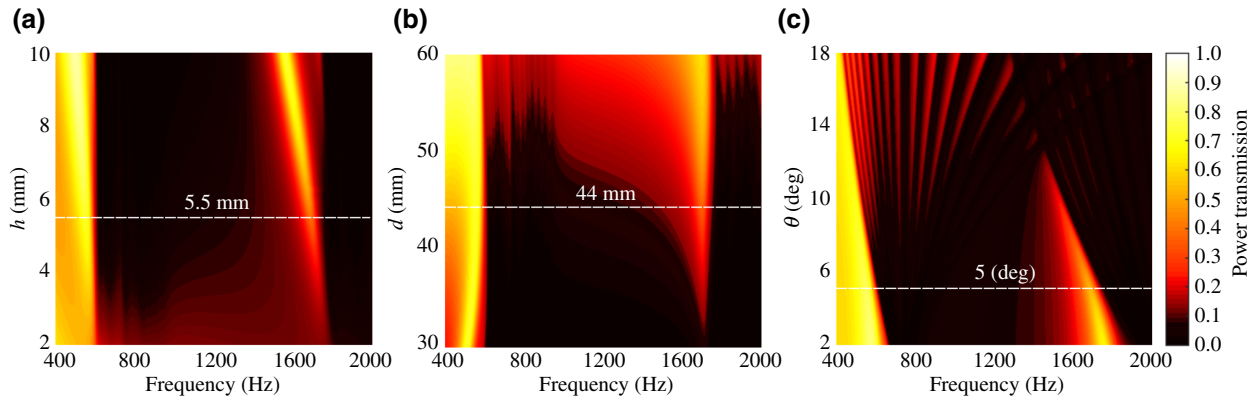


FIG. 3. Variation of power transmission with (a) the thickness of each layer h , (b) the inner diameter of the central orifice d , and (c) the angle shift of the partition blade from layer to layer θ . The dark regions represent effectively silenced zones. The dashed white lines in the color maps show the selected system parameters.

quasi-impedance-matching. At this point, the metaunit is working in a highly efficient absorption mode. In contrast, when a chamber is in a resonant state, but the dissipation rate can be ignored, the reradiation wave from the chamber interferes destructively with the incident wave and results in a quasi-Fano-resonance, where a strong reflection mode arises from the metaunit. Between these two extremes (i.e. a resonant state with an insufficient dissipation rate), the metaunit is in an intermediate state between the absorption mode and the reflection mode, where the coaction of dissipation and interference ensures its highly efficient sound blocking.

Through the above analysis, it is demonstrated that the consistently strong sound blocking comes from the coaction of the 16 coupled resonant chambers. Empowered by the synergistic effect, our hybrid-functional metasurface beats previous broadband designs that used only

interference [37,38] or absorption [35,39] by a large margin in the operating range.

E. Customizing the ventilation barrier

The designed barrier has potential for great flexibility in tailoring its acoustic behavior. Figure 3(a) shows the calculated power transmission as a two-dimensional color map of the thickness h and frequency. The bandwidth (power transmission less than 0.1) increases with the chamber thickness and stabilizes when h reaches 5.5 mm. A further increase in h results in little further increase of the bandwidth (see the width of the region in black). The opening rate of the ventilation barrier also has a marked impact on the performance of the ventilation barrier. Figure 3(b) shows the color map for various values of d , indicating

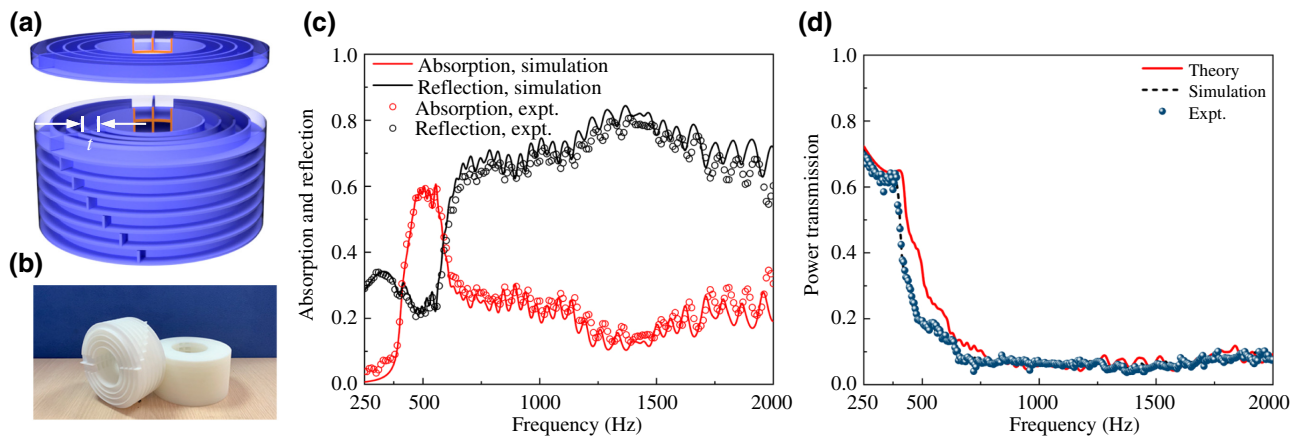


FIG. 4. (a) The modified metaunit featuring three additional circumferential partition blades in each layer. (b) A photograph of the three-dimensionally-printed specimen and its inner structure. (c) The numerically calculated absorption (red line) and reflection (black line) and the measured absorption (red circles) and reflection (black circles) of the metaunit. (d) Theoretical (red line), simulated (dashed black line), and measured (blue dots) power transmission of the metaunit ($D = 100$ mm, $d = 44$ mm, $h = 5.5$ mm, $b = 1$ mm, $H = 53$ mm, $\psi = 120^\circ$, $\theta = 8^\circ$, $S_n = 42.3$ mm², and $t = 1$ mm).

the trade-off between the ventilation efficiency and sound-proofing bandwidth. Here $d = 44$ mm is used as a balance for our design. More importantly, the 16 elaborate resonant chambers play a central role in determining the overall performance. To make them well detuned to collectively cover such a wide operating range, the angle shift of the partitions from layer to layer θ is the key factor. As illustrated by Fig. 3(c), for a modest angle shift ($2\text{--}8^\circ$), the bandwidth can be expanded or compressed accordingly by increasing or decreasing θ . For a larger θ , the broadband will decompose—namely, now the metaunit is serving as a frequency comb. In general, the above-mentioned characteristics, arising from the rich geometrical parameters, provide our design with adjustable frequency behavior and suggest an approach for the design of a ventilation barrier with a target-set spectrum.

F. The modified ventilation barriers toward ultrabroadband sound blocking

In the above design, the phase shift of the deflected blade from layer to layer results in 16 detuned resonant chambers that collectively guarantee a remarkable broadband performance. To further extend the working range of the metaunit without changing its profile (outer diameter D , inner diameter d , and overall thickness H), circumferential blades are deployed on each layer. As illustrated in Fig. 4(a), now the modified metaunit contains three circumferential blades evenly spaced (partition spacing t) on each layer. Compared with the prototype shown in Fig. 1(a), these circumferential partitions provide an additional degree of freedom, so there are eight detuned chambers on each layer and 64 in total. Figure 4(b) shows the sample of the modified metaunit made of photosensitive resin via 3D printing. This design, although it features

a more-complicated inner structure, has the same underlying working mechanism as its prototype. The numerical simulation and experimental results shown in Fig. 4(c) verify that the modified metaunit works via the synergy of dissipation and interference, where dissipation dominates at low frequencies (greater than 0.5 at 450–580 Hz), while interference is dominant at higher frequencies. The theoretical, numerical, and experimental data shown in Fig. 4(d) witness a substantially increased operating range: an effective blocking of more than 90% of incident sound energy from 650 Hz to 2000 Hz (experimental data). Compared with its prototype (628–1400 Hz), the additional circumferential partitions contribute mainly at higher frequencies.

In practice, the functionality of an acoustic barrier should not be restricted to only normal incidence. We numerically inspect the power transmission through the proposed acoustic barrier under oblique incidence (Fig. 5). The simulation results show that the broadband characteristic is observable under a wide range of the angle of incidence, while the sound blocking becomes even better under oblique incidence. Furthermore, although the designed metaunit is not axially symmetric, the deep-subwavelength nature in the frequency range considered ensures that its transmission properties will not be affected by the rotation angle ω of the incident wave (ω is illustrated in the inset in Fig. 5). This significantly expands the scope of the practicability of our design in harsh environments with background noise impinging from different directions.

To estimate the ventilation characteristics of the metaunit, experiments are performed. The inset in Fig. 6 shows the experimental setup. In the experiments, an electric fan is placed at the inlet of the waveguide, and the wind speed at the outlet is measured twice, with and without the presence of the designed metaunit. The measured ventilation

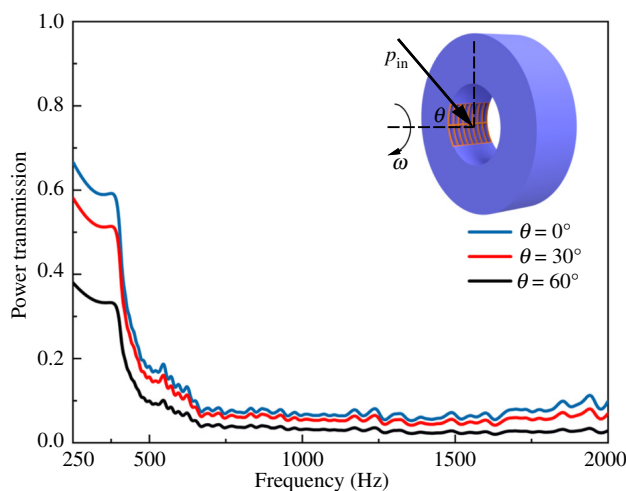


FIG. 5. Power transmission for illumination by a plane wave with incident angles of 0° (blue line), 30° (red line), and 60° (black line).

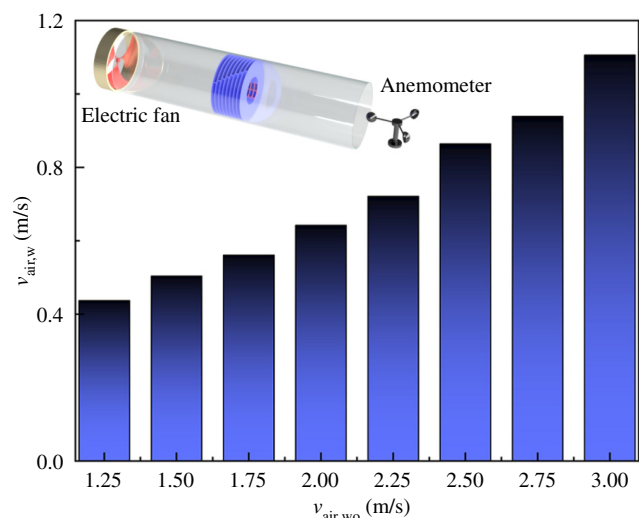


FIG. 6. The ventilation characterization system and the measured wind-velocity ratio.

performance, characterized by the wind-velocity ratios (the ratios between airflow velocities with and without the samples), is plotted in Fig. 6. The results manifest a linear dependence and a velocity ratio of around 34%, and demonstrate effective airflow circulation.

III. CONCLUSIONS

In summary, we conceptually propose and experimentally validate an ultrabroadband ventilation barrier via a hybrid-functional acoustic metasurface. In contrast to previous broadband designs, the synergistic effect from our hybrid-functional metasurface offers an efficient means to substantially increase the operating range. Experiments are conducted to validate the proposed design. The hybridization of dissipation and interference serves as a powerful tool to guarantee the remarkable broadband performance, enabling consistent blocking of more than 90% of incident energy in the range from 650 to 2000 Hz, while the structural thickness is only 53 mm (approximately $\lambda/10$). The rich geometrical parameters provide our design with adjustable frequency behavior. Our work opens up promising possibilities for shielding acoustic waves in such a compact yet open manner, and more essentially suggests an efficient route toward on-demand broadband impedance engineering in an open metasurface.

ACKNOWLEDGMENTS

This work was supported by the National Natural Science Foundation of China (Grants No. 11774265, No. 12074288, and No. 12074286) and the Shanghai Science and Technology Committee (Grants No. 20ZR1460900 and No. 20ZR1461700).

[1] J. Kang and M. W. Brocklesby, Feasibility of applying micro-perforated absorbers in acoustic window systems, *Appl. Acoust.* **66**, 669 (2005).

[2] X. Yu, S.-K. Lau, L. Cheng, and F. Cui, A numerical investigation on the sound insulation of ventilation windows, *Appl. Acoust.* **117**, 113 (2017).

[3] N. Yuya, N. Sohei, N. Tsuyoshi, and Y. Takashi, Sound propagation in soundproofing casement windows, *Appl. Acoust.* **70**, 1160 (2009).

[4] J. Zhu, J. Christensen, J. Jung, L. Martin-Moreno, X. Yin, L. Fok, X. Zhang, and F. J. Garcia-Vidal, A holey-structured metamaterial for acoustic deep-subwavelength imaging, *Nat. Phys.* **7**, 52 (2010).

[5] N. Kaina, F. Lemoult, M. Fink, and G. Lerosey, Negative refractive index and acoustic superlens from multiple scattering in single negative metamaterials, *Nature* **525**, 77 (2015).

[6] B. Liang, B. Yuan, and J. C. Cheng, Acoustic Diode: Rectification of Acoustic Energy Flux in One-Dimensional Systems, *Phys. Rev. Lett.* **103**, 104301 (2009).

[7] B. Liang, X. S. Guo, J. Tu, D. Zhang, and J. C. Cheng, An acoustic rectifier, *Nat. Mater.* **9**, 989 (2010).

[8] Y. Li, B. Liang, Z. M. Gu, X. Y. Zou, and J. C. Cheng, Reflected wavefront manipulation based on ultrathin planar acoustic metasurfaces, *Sci. Rep.* **3**, 2546 (2013).

[9] J. Zhao, B. Li, Z. Chen, and C. W. Qiu, Manipulating acoustic wavefront by inhomogeneous impedance and steerable extraordinary reflection, *Sci. Rep.* **3**, 2537 (2013).

[10] Y. Li, X. Jiang, R. Q. Li, B. Liang, X. Y. Zou, L. L. Yin, and J. C. Cheng, Experimental Realization of Full Control of Reflected Waves with Subwavelength Acoustic Metasurfaces, *Phys. Rev. Appl.* **2**, 064002 (2014).

[11] K. Tang, C. Qiu, M. Ke, J. Lu, Y. Ye, and Z. Liu, Anomalous refraction of airborne sound through ultrathin metasurfaces, *Sci. Rep.* **4**, 6517 (2014).

[12] J. Mei and Y. Wu, Controllable transmission and total reflection through an impedance-matched acoustic metasurface, *New J. Phys.* **16**, 123007 (2014).

[13] Y. Xie, W. Wang, H. Chen, A. Konneker, B. I. Popa, and S. A. Cummer, Wavefront modulation and subwavelength diffractive acoustics with an acoustic metasurface, *Nat. Commun.* **5**, 5553 (2014).

[14] Y. Li, X. Jiang, B. Liang, J. C. Cheng, and L. Zhang, Metascreen-Based Acoustic Passive Phased Array, *Phys. Rev. Appl.* **4**, 024003 (2015).

[15] C. Shen, Y. Xie, J. Li, S. A. Cummer, and Y. Jing, Asymmetric acoustic transmission through near-zero-index and gradient-index metasurfaces, *Appl. Phys. Lett.* **108**, 223502 (2016).

[16] Y. Li, C. Shen, Y. Xie, J. Li, W. Wang, S. A. Cummer, and Y. Jing, Tunable Asymmetric Transmission Via Lossy Acoustic Metasurfaces, *Phys. Rev. Lett.* **119**, 035501 (2017).

[17] B. Assouar, B. Liang, Y. Wu, Y. Li, J. C. Cheng, and Y. Jing, Acoustic metasurfaces, *Nat. Rev. Mater.* **3**, 460 (2018).

[18] X. Wang, X. Fang, D. Mao, Y. Jing, and Y. Li, Extremely Asymmetrical Acoustic Metasurface Mirror at the Exceptional Point, *Phys. Rev. Lett.* **123**, 214302 (2019).

[19] S. Fan, S. Zhao, A. Chen, Y. Wang, B. Assouar, and Y. Wang, Tunable Broadband Reflective Acoustic Metasurface, *Phys. Rev. Appl.* **11**, 044038 (2019).

[20] G. Ma, M. Yang, S. Xiao, Z. Yang, and P. Sheng, Acoustic metasurface with hybrid resonances, *Nat. Mater.* **13**, 873 (2014).

[21] Y. Li and B. M. Assouar, Acoustic metasurface-based perfect absorber with deep subwavelength thickness, *Appl. Phys. Lett.* **108**, 063503 (2016).

[22] S. Huang, X. Fang, X. Wang, B. Assouar, Q. Cheng, and Y. Li, Acoustic perfect absorbers via spiral metasurfaces with embedded apertures, *Appl. Phys. Lett.* **113**, 233501 (2018).

[23] S. Huang, X. Fang, X. Wang, B. Assouar, Q. Cheng, and Y. Li, Acoustic perfect absorbers via helmholtz resonators with embedded apertures, *J. Acoust. Soc. Am.* **145**, 254 (2019).

[24] S. Huang, Z. Zhou, D. Li, T. Liu, X. Wang, J. Zhu, and Y. Li, Compact broadband acoustic sink with coherently coupled weak resonances, *Sci. Bull.* **65**, 373 (2020).

[25] N. Jiménez, V. Romero-García, V. Pagneux, and J.-P. Groby, Rainbow-trapping absorbers: Broadband, perfect

- and asymmetric sound absorption by subwavelength panels for transmission problems, *Sci. Rep.* **7**, 13595 (2017).
- [26] N. Jiménez, V. Romero-García, V. Pagneux, and J.-P. Groby, Quasiperfect absorption by subwavelength acoustic panels in transmission using accumulation of resonances due to slow sound, *Phys. Rev. B* **95**, 014205 (2017).
- [27] H. Long, Y. Cheng, and X. Liu, Asymmetric absorber with multiband and broadband for low-frequency sound, *Appl. Phys. Lett.* **111**, 143502 (2017).
- [28] L. J. Li, B. Zheng, L. M. Zhong, J. Yang, B. Liang, and J. C. Cheng, Broadband compact acoustic absorber with high-efficiency ventilation performance, *Appl. Phys. Lett.* **113**, 103501 (2018).
- [29] X. Wu, K. Y. Au-Yeung, X. Li, R. C. Roberts, J. Tian, C. Hu, Y. Huang, S. Wang, Z. Yang, and W. Wen, High-efficiency ventilated metamaterial absorber at low frequency, *Appl. Phys. Lett.* **112**, 103505 (2018).
- [30] C. Shen, Y. Xie, J. Li, S. A. Cummer, and Y. Jing, Acoustic metacages for sound shielding with steady air flow, *J. Appl. Phys.* **123**, 124501 (2018).
- [31] H. L. Zhang, Y. F. Zhu, B. Liang, J. Yang, J. Yang, and J. C. Cheng, Omnidirectional ventilated acoustic barrier, *Appl. Phys. Lett.* **111**, 203502 (2017).
- [32] R. Ghaffarivardavagh, J. Nikolajczyk, S. Anderson, and X. Zhang, Ultra-open acoustic metamaterial silencer based on fano-like interference, *Phys. Rev. B* **99**, 024302 (2019).
- [33] X. Wang, X. Luo, B. Yang, and Z. Huang, Ultrathin and durable open metamaterials for simultaneous ventilation and sound reduction, *Appl. Phys. Lett.* **115**, 171903 (2019).
- [34] J. W. Jung, J. E. Kim, and J. W. Lee, Acoustic metamaterial panel for both fluid passage and broadband soundproofing in the audible frequency range, *Appl. Phys. Lett.* **112**, 041903 (2018).
- [35] X. Xiang, X. Wu, X. Li, P. Wu, H. He, Q. Mu, S. Wang, Y. Huang, and W. Wen, Ultra-open ventilated metamaterial absorbers for sound-silencing applications in environment with free air flows, *Extreme Mech. Lett.* **39**, 100786 (2020).
- [36] H. Nguyen, Q. Wu, X. Xu, H. Chen, S. Tracy, and G. Huang, Broadband acoustic silencer with ventilation based on slit-type Helmholtz resonators, *Appl. Phys. Lett.* **117**, 134103 (2020).
- [37] M. Sun, X. Fang, D. Mao, X. Wang, and Y. Li, Broadband Acoustic Ventilation Barriers, *Phys. Rev. Appl.* **13**, 044028 (2020).
- [38] J. Yang, J. S. Lee, H. R. Lee, Y. J. Kang, and Y. Y. Kim, Slow-wave metamaterial open panels for efficient reduction of low-frequency sound transmission, *Appl. Phys. Lett.* **112**, 091901 (2018).
- [39] S. Kumar and H. P. Lee, Labyrinthine acoustic metastructures enabling broadband sound absorption and ventilation, *Appl. Phys. Lett.* **116**, 134103 (2020).